A vibrational in vitro approach to evaluate the potential of monoolein nanoparticles as isofuranodiene carrier in MDA-MB 231 breast cancer cell line: new insights from Infrared and Raman microspectroscopies

note finali coverpage

(Article begins on next page)

06 October 2024

A vibrational *in vitro* approach to evaluate the potential of monoolein nanoparticles as isofuranodiene carrier in MDA-MB 231 breast cancer cell line: new insights from Infrared and Raman microspectroscopies

Valentina Notarstefano,[a,1] Michela Pisani,[b,1] Massimo Bramucci,[c] Luana Quassinti,[c] Filippo Maggi,[c] Lisa Vaccari,[d] Marco Parlapiano,[b] Elisabetta Giorgini,[a,*] Paola Astolfi.[b,*]

[a] Department of Life and Environmental Sciences, Università Politecnica delle Marche, Via Brecce Bianche, 60131 Ancona (Italy)

[b] Department of Materials, Environmental Sciences and Urban Planning, Università Politecnica delle Marche, Via Brecce Bianche, 60131 Ancona (Italy)

[c] School of Pharmacy, University of Camerino, I-62032 Camerino, Italy

[d] Elettra Sincrotrone Trieste, SISSI Beamline, s.s. 14 km 163,500 in Area Science Park, 34149 Basovizza , Trieste (Italy)

*Address correspondence to Elisabetta Giorgini e.giorgini@univpm.it and Paola Astolfi p.astolfi@univpm.it

[1] These authors contributed equally to this article

Authors: e-mail v.notarstefano@staff.univpm.it, m.pisani@univpm.it, massimo.bramucci@unicam.it; luana.quassinti@unicam.it; filippo.maggi@unicam.it; lisa.vaccari@elettra.eu; m.parlapiano@staff.univpm.it

1

ABSTRACT

Isofuranodiene (IFD) is a sesquiterpene occurring in several plant species, which proved to have multiple anticancer activities. IFD has a lipophilic nature and, hence, a very low water solubility and a poor bioavailability; moreover, it is not stable, undergoing the "Cope rearrangement" to the less active curzerene. The use of appropriate delivery systems can thus be considered as a valid tool to enhance IFD bioavailability, solubility, stability and at the same time also to improve its intracellular uptake and pharmacological activity. Within this frame, monoolein (GMO) nanoparticles loaded with IFD were prepared and their enhanced anticancer activity, compared to pristine IFD, was assessed. In this study, for the first time, an *in vitro* Fourier Transform Infrared and Raman Microspectroscopy approaches were exploited to evaluate the effects of IFD, alone and loaded in GMO nanoparticles, on MDA-MB 231 breast cancer cell line. The anti-cancer effects of IFD were evidenced by both the spectroscopic techniques and discriminated from the GMO-induced changes in the culture environment; moreover, a synergistic effect of IFD and GMO administration can be envisaged by the experimental results.

Keywords: Isofuranodiene, monoolein nanoparticles, MDA-MB 231 cells, Fourier Transform Infrared Microspectroscopy, Raman Microspectroscopy, chemometrics.

1. Introduction

The use of plants and plant extracts for the treatment of different diseases continues to expand rapidly with over three quarters of the world's population resorting to these products in case of most varied pathologies. Plant extracts, which are mainly obtained from leaves, fruits, stems or roots, are complex mixtures of chemical compounds with multiple biological and therapeutical activities, such as antioxidant, antibiotic, antidiabetic, anti-inflammatory, anticancer, and others [1,2]. Among these compounds there is isofuranodiene (IFD), a sesquiterpene occurring in several species of the genera *Curcuma* and *Commiphora* and obtained also from the essential oil of *Smyrnium olusatrum*

(Apiaceae) [3,4]; IFD has been proved to have multiple anticancer activities, as a result of the modulation of several cellular processes, including apoptosis triggering, ROS production, DNA fragmentation and cell cycle arrest in G2/M phase [5–10]. IFD is a lipophilic compound (LogP = 3.52 [11]) with a very low water solubility [12] and this may result in a poor bioavailability; moreover, IFD is unstable undergoing the "Cope rearrangement" to the less active curzerene [13]. It follows that appropriate delivery systems can be considered as valid tools to enhance IFD bioavailability, solubility, stability and at the same time also to improve its intracellular uptake and pharmacological activity. Lipid-based nanocarriers, such as nano- and micro-emulsions [14,15], nanostructured lipid carriers [11] and, recently, structured liquid crystalline nanoparticles have been considered and successfully tested for IFD encapsulation and delivery [16]. In particular, in our recent paper, IFD-monoolein nanoparticles were prepared and characterized [16]. Monoolein is an amphiphilic molecule which, in the presence of excess water, self-assembles in a series of liquid crystalline structures ordered in one or three dimensions, as a function of water concentration, with the polar portions oriented towards the aqueous milieu whereas the hydrophobic portions cluster together to reduce the exposure to water [17]. Typically, at room temperature and as a function of water concentration, monoolein self assembles in inverted cubic phases, in the gyroid *Ia3d* and in the diamond *Pn3m* space groups, whereas the primitive *Im3m* cubic phase is formed in the presence of additives such the steric stabilizer Pluronic® F127 [18]. Addition of other additives [19–22] or drug encapsulation [23] may determine, according to their lipophilicity, the transition to a more curved mesophase such the inverted hexagonal one *H_{II}*, as in the case of IFD [16].

Monoolein bulk phases are of limited interest in the drug delivery field because of their viscosity and difficult handling but, upon fragmentation in the presence of the stabilizer, they can be obtained as nanoparticles, cubosomes and hexosomes. These latter structures are able to incorporate high amount of both lipophilic and hydrophilic drugs because of their ordered internal structures and large interfacial surface, to protect the loaded cargo from hydrolysis, oxidation or enzymatic degradation and to improve their bioavailability, thus representing efficient and promising delivery vectors for

small drugs [24,25], peptides and proteins [26,27], nucleic acids [28,29]. Within this frame, different anticancer agents have been encapsulated in cubic nanoparticles, composed of monoolein or other amphiphilic molecules such as phytantriol; their activity has been tested in several cell lines and proved to be higher after the encapsulation in the nanoparticles, with respect to the free drug [30–35]. The assessment of cell viability is usually performed by the colorimetric MTT (3-[4,5-dimethylthiazol-2-yl]-2,5 diphenyl tetrazolium bromide) [36], or Trypan Blue [37] assays, which are cheap and easy procedures giving information on cell survival, disregarding the mechanism responsible for cell death. At this regard, the spectral information deriving from Fourier Transform Infrared (FTIRM) and Raman (RMS) microspectroscopies may shed new light on the mechanisms by which cells respond to the treatments. In fact, these techniques are successfully exploited to investigate the chemical composition and structure of the cellular macromolecules based on the position, intensity and width of their main bands, allowing to highlight even tiny alterations [38,39]. The changes, affecting lipids, proteins, carbohydrates or nucleic acids, can be associated to the main biological processes such as apoptosis, necrosis, etc. More in detail, FTIRM and RMS are mutually complementary techniques, differing in the physical phenomena they rely on: polar group vibrations are detected by IR absorption, while polarizable ones are visible by Raman scattering. Hence, from the combination of both these techniques a deeper understanding of the biological sample is possible. Moreover, FTIRM has been applied for the analysis of small groups of hydrated cells, setting the spatial resolution to 30x30 μm^2, whereas confocal Raman microscopic resolutions close to 1 μm could be achieved with a ×100 objective. Thus, from FTIRM an information deriving from averaging larger areas is obtained, while RMS enables single-cell analyses, thus permitting to focus on subcellular compartments [40].

In the present study, for the first time, an *in vitro* FTIRM and RMS approach was performed on MDA-MB 231 cells, treated with IFD loaded into GMO nanoparticles (Chart 1). The aim was to

elucidate the mechanism of action of IFD and the effective advantages of GMO nanoparticles as nanocarriers to enhance the anticancer activity of IFD.

Chart

2. Experimental section

2.1 Chemicals

Isofuranodiene IFD was isolated from the essential oil of *Smyrnium olusatrum L.* inflorescences by crystallization following the procedure described in ref. [41] and [12]. Glyceryl monooleate (Monomuls® 90-O 18,) was kindly provided from BASF (Germany). Pluronic® F127 (PEO_{98}-PPO_{67}-PEO_{98}) and all the used solvents were purchased from Sigma-Aldrich (Milan, Italy). Milli-Q water was used for the preparation of all the samples.

2.2 Nanostructured lipid dispersions preparation and characterization

Monomuls® 90-O 18 (50 mg) and Pluronic® F127 (8% w/w) were dissolved in chloroform (hereinafter, this sample is named GMO and the presence of the stabilizer is implied). The solvent was evaporated under a gentle steam of nitrogen and, subsequently, under vacuum for 2 h. For the IFD loaded system (GMO+IFD), 4 mg of IFD were added to the mixture before solvent evaporation. In both cases, the dried residue was hydrated with 300 μL of water and the obtained gels were left to equilibrate for 24 h at room temperature. Water (2200 μL) was added to GMO and GMO+IFD bulk phases to have a concentration of 20 mg/mL lipid/water and 1.6 mg/mL IFD and nanodispersions were obtained after 10 min probe sonication in pulse mode (1 s on 1 s off, 50% maximum amplitude). Phase identity of the obtained nanoparticles was determined by synchrotron X-ray scattering performed at the SAXS beamline, Elettra Sincrotrone Trieste (Trieste, Italy). 2D diffraction patterns were recorded on a Dectris Pilatus 1M detector using a 1.54 Å wavelength (8 keV incident beam energy) at 1279 mm from the sample which covered a q range of 0.15-5 nm^{-1} ($q = 4\pi \sin\theta/\lambda$, where 2θ

is the scattering angle and λ the wavelength). A vacuum chamber was placed between the sample and the detector to remove the air scattering, whereas radiation damage of the samples was reduced by using a maximum exposure time of 1s. The 2D spectra were integrated to have a 1D intensity *versus* q patterns. From the linear fit of the plot q_{hkl} *vs* $\sqrt{h^2 + k^2 + l^2}$ and q_{hkl} *vs* $\sqrt{h^2 + k^2 + hk}$ the lattice parameters *a* for the cubic and hexagonal phase were obtained, respectively.

2.3 Cell culture

Human breast adenocarcinoma cells (MDA-MB 231) were obtained from American Type Culture Collection (Rockville, MD). Cells were grown at 37 °C in a humidified atmosphere with 5% CO_2 in Dulbecco's Modified Eagle's Medium (DMEM) with 2 mM L-glutamine, 100 IU/mL penicillin, 100 µg/mL streptomycin (Corning, Manassas, VA, USA), and supplemented with 10 % heat-inactivated fetal bovine serum (HI-FBS) (Corning, Manassas, VA, USA). Cells were maintained in culture by selective trypsinisation with trypsin/EDTA solution (0.05% trypsin–0.02% EDTA) and diluted in fresh medium before reaching the 80 % of confluence state.

2.4 Cell treatment

Exponentially growing cells were seeded in duplicate at the density of 0.72×10^6 cells into 6-well tissue culture plates (Corning Incorporated, NY, USA) in complete medium and incubated at 37 °C with a 5% CO_2 atmosphere for 24 h. Cells were then treated for 24 and 48 h with 116.9 µg/mL GMO and 79.9 µg lipid/mL GMO+IFD nanoparticles corresponding to the IC_{50} values, previously determined in [16] for the empty and loaded systems, respectively and with 8.1 µg/mL IFD equal to the amount of the drug present in the 79.9 µg lipid/mL GMO+IFD complex. Other aliquots, used as control groups (Ctrl-), were normally cultured without any treatment for the same exposure times. The following experimental groups were collected: Ctr-24, Ctrl-48, IFD-24, IFD-48, GMO-24, GMO-48, GMO+IFD-24 and GMO+IFD-48 experimental groups. At each time point, medium was removed and stored to collect floating cells; then, 100 µL of 0.05% trypsin/EDTA solution was added

into each well and incubated for 5 min. After cell detachment, the medium with floating cells was added back to the trypsinised cells, and 500 µL of fresh supplemented medium were added. The cell suspension was then centrifuged at 100xg for 5 min at 4 °C. The cellular pellet was rinsed with PBS. Cells were fixed in a 4% paraformaldehyde (PFA) solution for 30 min and then centrifuged at 100xg for 5 min; the pellet was washed 3 times in physiological solution and maintained at 4 °C. This procedure has been validated to retain the biochemical profile of the cells as close as possible to that of live cells [42], preserving hydration, and protecting them from biological damage during shipping [40,43].

2.5 FTIRM measurements and data analysis

FTIRM measurements were performed in duplicate at the Chemical and Life Sciences branch of the Infrared Beamline SISSI (Synchrotron Infrared Source for Spectroscopic and Imaging), Elettra Sincrotrone Trieste (Trieste, Italy) (Proposal N. 20190118). A Hyperion 3000 Vis-IR microscope coupled with a Vertex 70V interferometer and equipped with a HgCdTe (MCT_A) detector was used (Bruker Optics, Ettlingen, Germany).

Pellets were resuspended with 15 µL of 0.9 % NaCl physiological solution, and deposited, without any further treatment, into a specific in-house built biocompatible IR transparent microfluidic device for *in vitro* FTIRM analysis. The device, available at SISSI-Bio beamline, comprises two CaF_2 optical windows (0.5 mm thick, 13- and 10-mm diameter, respectively), spaced apart 7.5 µm [44]. For each sample, ~100 microareas (30×30 µm^2) containing 3-4 densely packed cells were selected by visible microscopy. On these areas, IR spectra were collected in transmission mode in the MIR region (4000–800 cm^{-1}), averaging 512 scans (spectral resolution 4 cm^{-1}, zero-filling factor 2, scanner velocity 40 kHz). Before each sample acquisition, a background spectrum was acquired on a clean CaF_2 window, while a 0.9 % NaCl physiological solution spectrum was collected each 10 cells spectra: in both cases, the same parameters for cell acquisition were used.

All the collected raw spectra were corrected for the contribution of atmospheric carbon dioxide with the Atmospheric Compensation routine of OPUS 7.5 software (Bruker Optics GmbH, Ettlingen, Germany). Hence, the spectral contributions of the aqueous medium were subtracted by running an in-house built Matlab algorithm, based on the optimization of the baseline flatness in the $2500-1850$ cm^{-1} range containing the water combination band [38,44]. IR spectra showing a peak height at 1660 cm^{-1} (Amide I band of proteins) lower than 0.07 a.u. were discarded. The remaining spectra were vector-normalised and converted in Second Derivative mode (Savitzky-Golay filter, 9 points of smoothing) (OPUS 7.5 software, Bruker Optics GmbH, Ettlingen, Germany).

These pre-processed spectra were then subjected to multivariate analysis, with no further processing. More in detail, pairwise Principal Components Analysis (PCA) of second derivatives of pre-processed spectra of all experimental groups was performed (Ctrl-24/IFD-24, Ctrl-48/IFD-48, Ctrl-24/GMO-24, Ctrl-48/GMO-48, Ctrl-24/GMO+IFD-24, and Ctrl-48/GMO+IFD-48); PC scores and loadings were considered (OriginPro 2018b, OriginLab Corporation) [45].

The average absorbance spectra and the corresponding average absorbance spectra $\pm$ standard deviation (S.D.) spectra of al experimental groups were calculated in the $3050-2800$ cm^{-1} and $1800-900$ cm^{-1} spectral regions. Spectra curve fitted in the $1350-1000$ cm^{-1} spectral region, upon straight baseline correction and vector normalization. The number and position of the underlying bands were identified by second derivative minima analysis and fixed during fitting procedure with Gaussian functions (GRAMS/AI 9.1, Galactic Industries, Inc., Salem, New Hampshire). The integrated areas (A) of the underlying bands were used to calculate the following band area ratios: A_{1319}/A_{TOT}, A_{1054}/A_{TOT}, A_{1240}/A_{1221}, A_{1120}/A_{TOT}, A_{1087}/A_{TOT}, and A_{967}/A_{TOT}. A_{TOT} was calculated as the sum of the integrated areas of all the underlying bands in the $1350-900$ cm^{-1} spectral range.

2.5 RMS measurements and data analysis

RMS measurements were performed in duplicate at the Laboratory of Advanced Research Instrumentation, Department of Life and Environmental Sciences, Università Politecnica delle

Marche (Ancona, Italy). A Horiba Jobin-Yvon XploRA Raman microspectrometer, equipped with a 532-nm diode laser (~50mW laser power at the sample) was used as source. All measurements were acquired by using a ×100 objective (Olympus, Japan). The spectrometer was calibrated to the 520.7 cm^{-1} line of silicon prior to spectral acquisition. A 600 lines per mm grating was chosen. A 100 μm confocal pinhole was used for all measurements. The spectra were dispersed onto a 16-bit dynamic range Peltier cooled CCD detector. The spectral range from 400 to 1800 cm^{-1} was chosen and spectra were acquired for 3×10 seconds at each spot.

Cells were grown onto normal glass coverslips in 6-well tissue culture plates for 24 and 48 h in the same condition reported for FTIRM (Ctrl-24, Ctrl-48, IFD-24, IFD-48, GMO-24, GMO-48, GMO+IFD-24 and GMO+IFD-48 experimental groups). At each time point, the medium was removed, and the coverslips were rinsed twice with PBS. Cells were fixed in a 4% paraformaldehyde (PFA) solution for 10 min, washed twice in physiological solution, and stored at 4°C.

For each cellular sample, 10 point/spectra were acquired from ~20 single cells seeded on the glass slide, on the nuclear and perinuclear regions; for each single cell, the average RMS spectrum was calculated (Averaging routine OPUS 7.5 software, Bruker Optics GmbH, Ettlingen, Germany). Raman spectra displayed homogeneous profiles; no contribution of glass to the spectra was observed. Raman spectra were smoothed using 9 smoothing points, baseline-corrected with the polynomial method (2 iterations) (OPUS 7.5 software, Bruker Optics GmbH, Ettlingen, Germany), and then submitted to multivariate analysis. As described for FTIRM analysis, pairwise PCA of pre-processed spectra of all experimental groups was performed (Ctrl-24/IFD-24, Ctrl-48/IFD-48, Ctrl-24/GMO-24, Ctrl-48/GMO-48, Ctrl-24/GMO+IFD-24, and Ctrl-48/GMO+IFD-48); PC scores and loadings were considered (OriginPro 2018b, OriginLab Corporation) [45].

To quantify the identified alterations due to treatments, the height (I) of some selected peaks of interest was calculated (Integration mode K, OPUS 7.5 software).

2.6 Statistical analysis

Normally distributed data deriving from FTIRM and RMS spectra were presented as mean ± S.D. Significant differences between experimental groups were determined by means of a factorial analysis of variance (one-way ANOVA), followed by Tukey's multiple comparisons test, by the statistical software Prism6 (Graphpad Software, Inc. USA). One-way ANOVA compares the means of Ctrl-24, Ctrl-48, IFD-24, IFD-48, GMO-24, GMO-48, GMO+IFD-24, and GMO+IFD-48 groups to make inferences about the population means. Statistical significance was set at $p < 0.05$. Different letters over box charts indicate statistically significant differences among the above defined experimental groups.

3. Results

3.1 Nanoparticles characterization

Colloidal dispersions of GMO, empty and loaded with IFD, were prepared by sonication of the viscous bulk phases formed upon hydration of GMO and GMO+IFD in the presence of a steric stabilizer such as the triblock copolymer Pluronic® F127. The internal structure of the dispersed systems was verified using small-angle X-ray scattering (Fig. 1): an *Im3m* inverse cubic phase with a lattice constant a = 13.40 nm was observed for the empty dispersion as indicated by the typical Bragg peaks (110), (200), (211) which changed to a reverse hexagonal H_{II} phase characterized by the (100), (110), (200) peaks and by a lattice parameter a = 6.25 nm when IFD was encapsulated in the lipid matrix.

Figure 1

This same transition was already observed when the systems GMO and GMO+IFD were studied in the bulk phase [16] and no differences should have been expected between the cubic or hexagonal gel phase and the corresponding cubosomes and hexosomes [46]. Monoolein, together with phytantriol, is one of the most frequently investigated amphiphiles able to form reverse phases with a negative curvature (hexagonal and cubic) in excess water because of their wedge-shaped molecules

10

[47]. In particular, in the presence of the steric stabilizer F127, as in the cases of our samples, it adopts an *Im3m* phase consisting of a complex 3-D lipid bilayer wrapped around two intertwined and unconnected water networks [48], as in the other bicontinuous cubic mesophases *Pn3m* and *Ia3d*, but with the characteristic that water channels meet at 90° in 6-way junctions [47].

Incorporation of the lipophilic IFD molecule (logP = 3.52 [11]) in the lipid matrix determined an increase of the volume of its hydrophobic portion and of its negative curvature, thereby forcing the cubosomes to transform into hexosomes having a mean particle size of ca. 176 nm and a surface potential of ca. -25 mV as determined in [16].

3.2 FTIRM analysis

The average IR spectra of Ctrl, IFD, GMO and GMO+IFD cellular groups collected both after 24 and 48 h of treatment are reported in Figs. 2A and 2B, respectively. Spectra are shown in the 3050-2800 cm^{-1} (lipid region) and the 1800-900 cm^{-1} (proteins and nucleic acids region) spectral ranges. In all experimental groups, the following bands were detected: 3010 cm^{-1}, 2926 cm^{-1} and 2865 cm^{-1} (stretching vibrations of C-H in unsaturated and saturated lipid alkyl chains) [49]; 1744 cm^{-1} (stretching vibration of C=O ester moiety in fatty acids) [50]; 1653 cm^{-1} and 1548 cm^{-1} (Amide I and II bands of proteins) [51]; 1457 cm^{-1} and 1400 cm^{-1} (bending vibrations of CH$_3$ and CH$_2$ groups in lipid alkyl chains) [51]; 1237 cm^{-1} (asymmetric stretching vibration of PO$_2^-$) [40]; 1166 cm^{-1} (stretching vibrations of C-C, C-O-C and C-OH groups in glycosylated compounds) [52]; 1089 cm^{-1} (symmetric stretching vibration of PO$_2^-$) [38], and 979 cm^{-1} (backbone vibrations of DNA) [39].

Figure 2

To evaluate differences due to treatments among the spectral profiles of all experimental groups, multivariate analysis was performed on second derivative pre-processed spectra in the 3050-2800 cm^{-1} and 1350-900 cm^{-1} Regions of Interest (ROI). The 1800-1350 cm^{-1} spectral range was not considered, since the water subtraction procedure inevitably affects the reliability of the spectral information. PCA was first carried out on Ctrl-24 and Ctrl-48 cell populations: no segregation was

found according to either PC1 or PC2 confirming the homogeneity and stability of control groups (data not shown). Then, the pairwise PCA analyses and corresponding PC1 loadings of IR second derivative pre-processed spectra of Ctrl-24/IFD-24, Ctrl-48/IFD-48, Ctrl-24/GMO-24, Ctrl-48/GMO-48, Ctrl-24/GMO+IFD-24, and Ctrl-48/GMO+IFD-48 cellular groups were performed in the same above defined ROIs (Figs. 3 and 4, respectively). In cell samples treated with IFD, an increasing segregation trend along PC1 axis was observed with respect to Ctrl populations at 24 and 48 h (Ctrl-24/IFD-24, 33.8% explained variance, Fig. 3A; Ctrl-48/IFD-48, 39.9% explained variance, Fig. 3B). A more evident separation was found between Ctrl and GMO samples, alone and loaded with IFD, both at 24 and 48 h, as highlighted by the scores plots of Ctrl-24/GMO-24 (67.8% explained variance, Fig. 3C), Ctrl48/GMO-48 (70.1% explained variance, Fig. 3D), Ctrl-24/GMO+IFD-24 (73.5% explained variance, Fig. 3E), and Ctrl48/GMO+IFD-48 (91.4% explained variance, Fig. 3F). Interestingly, all the pairwise PCA scatter plots highlighted a wider distribution of spectra from treated cell populations respect to control ones; moreover, an increase of the explained variance was found at 48 h with respect to 24 h. The analysis of PC1 loadings pinpointed among all the PCA comparisons, spectral modifications ascribable to lipids, nucleic acids and carbohydrates (Fig. 4).

Figure 3

Figure 4

For a deeper analysis of the information from loadings of second derivative spectra, the average absorbance spectra of Ctrl-24, Ctrl-48, IFD-24, IFD-48, GMO-24, GMO-48, GMO+IFD-24, and GMO+IFD-48 cell samples and their corresponding average $\pm$ SD spectra were fitted in the 1350-900 cm^{-1} region, representative of nucleic acids and carbohydrates, and also including Amide III of proteins; the position of the underlying bands, obtained by the analysis of minima in second derivative spectra, is reported in Table 1, together with the corresponding vibrational modes and bio-chemical assignments. The 3050-2800 cm^{-1} spectral region, representative of lipids, was not considered in this analysis given the huge contribution of GMO to the spectral profile. Also, the 1780-1480 cm^{-1} spectral

region, referred to Amide I and II bands of proteins, was not considered, since inevitably influenced by water subtraction procedure.

TABLE 1. Center position (wavenumber, cm^{-1}), vibrational mode and biochemical assignment of the underlying bands identified by second derivative minima analysis of average and average ± S.D. absorbance spectra of Ctrl-24, Ctrl-48, IFD-24, IFD-48, GMO-24, GMO-48, GMO+IFD-24, and GMO+IFD-48 in the 1350-900 cm^{-1} spectral range.

Wavenumber (cm^{-1})	Vibrational mode and biochemical assignment
~1319	Amide III band components of proteins (cellular proteins) [52]
~1240	Asymmetric stretching vibrations of phosphate moieties mainly of phospholipids and nucleic acids [53]
~1221	Asymmetric stretching vibrations of phosphate moieties of B-form DNA [54–56]
~1171	Stretching vibration of C-C, C-O-C and C-OH groups in glycosylated compounds [38,39]
~1120	Stretching vibration of the skeletal structure around the C2−OH group of RNA and NTPs [39,52,53]
~1087	Symmetric stretching vibrations of phosphate moieties in nucleic acids [53,57]
~1054	Stretching vibration of C-OH groups in carbohydrates and glycosylated compounds [52]
~1025	Stretching vibration of CH_2-OH moieties in carbohydrates and glycosylated compounds [38,39,58]
~967	Backbone vibrations of nucleic acids, mainly double-strand DNA [51–53]

Specific band area ratios were calculated and statistically analysed. The A_{1319}/A_{TOT} ratio (Amide III, representing the total proteins; Fig. 5A) displayed significantly lower values in all the treated groups, with a slight, but significant decrease in IFD-24 and IFD-48 groups; the lowest values were found in GMO and GMO+IFD-48 groups. The A_{1054}/A_{TOT} (representing the C–OH groups in carbohydrates and glycosylated compounds; Fig. 5B) ratio showed significantly lower values in IFD and GMO+IFD groups, respect to Ctrl and GMO, at both 24 and 48 h. As regards nucleic acids, the A_{1240}/A_{1221} (representing the ratio between the disordered A-form and the B-form of DNA; Fig. 5C), A_{1120}/A_{TOT} (representing RNA; Fig. 5D), A_{1087}/A_{TOT} (representing nucleic acids; Fig. 5E), and A_{967}/A_{TOT} (representing DNA; Fig. 5F) ratios were analysed; respect to Ctrl, both at 24 and 48 h, a significant increase of the A_{1240}/A_{1221} ratio was found in IFD and GMO+IFD groups, while no significant change was observed in GMO-24 and GMO-48; the A_{1120}/A_{TOT} ratio displayed significantly lower values in all the groups treated with IFD, with and without GMO, with the lowest values displayed by GMO+IFD-24 and GMO+IFD-48 groups; finally, no significant change among

13

the experimental groups at 24 h of treatment was displayed by the A_{1087}/A_{TOT} and A_{967}/A_{TOT} ratios, while a significant decrease was observed in IFD-48 and GMO+IFD-48 groups, respect to Ctrl-48.

Figure 5

3.3 RMS analysis

To focus the study on the nuclear and perinuclear regions, the single-cell analysis was also performed on the same experimental groups by RMS. The average Raman spectra of Ctrl, IFD, GMO and GMO+IFD both at 24 and 48 h are showed in Fig. 6 in the 400-1800 cm^{-1} spectral range. The Raman shift of the most relevant peaks, together with the vibrational mode and the biochemical assignment are reported in Table 2, with appropriate references.

Figure

TABLE 2. Center position (Raman shifts, cm^{-1}), vibrational mode and biochemical assignment of the peaks identified in average and average ± S.D. absorbance spectra of Ctrl-24, Ctrl-48, IFD-24, IFD-48, GMO-24, GMO-48, GMO+IFD-24, and GMO+IFD-48 in the 400-1800 cm^{-1} spectral region.

Raman shift (cm^{-1})	Vibrational mode and biochemical assignment
~1740	Stretching vibration of ester C=O groups of lipid esters [59,60]
~1652	Stretching vibration of amidic C=O groups of proteins (Amide I); stretching vibration of C=C bonds of glycerol monooleate (GMO) [40,61]
~1578	Stretching vibration of C=C bond in furan ring (IFD); ring breathing modes of guanine and adenine of DNA/RNA [60,62,63]
~1440	CH$_2$ bending modes of lipid chains; bending vibrations of CH$_2$ of glycerol monooleate [39,60]
~1340	Ring breathing modes of adenine and guanine of DNA/RNA [39,60,64]
~1298	CH$_3$/CH$_2$ twisting or bending mode of lipids [60,65]
~1250	=CH vibrations of unsaturated lipid chains [66,67]
~1084	Symmetric PO$_2^-$ stretching vibration of nucleic acids [60,68]
~1002	Symmetric stretching breathing vibration of phenylalanine [39,40]
~915	Ribose vibrations in RNA [60,69]
~833	O-P-O asymmetric stretching of B-form DNA [39,64,68]
~815	Stretching of RNA O-P-O phosphodiester bond (RNA) [67,70]
~785	O-P-O stretching of DNA backbone [71,72]

As observed in FTIRM analysis, PCA performed on all the spectra of Ctrl-24 and Ctrl-48 cell populations did not show any segregation according to either PC1 or PC2, confirming the homogeneity of control groups (data not shown). Then, the pairwise PCA analyses together with the

corresponding PC1 loadings of Raman pre-processed spectra of Ctrl-24/IFD-24, Ctrl-48/IFD-48, Ctrl-24/GMO-24, Ctrl-48/GMO-48, Ctrl-24/GMO+IFD-24, and Ctrl-48/GMO+IFD-48 groups were performed in the entire spectral range (Figs. 7 and 8, respectively). A clear segregation was found in all the pairwise PCA scores plots, even if more pronounced in GMO and GMO+IFD treated samples. In fact, Ctrl-24/IFD-24 (Fig. 7A) and Ctrl-48/IFD-48 (Fig. 7B) showed explained variances respectively of 77.8% and 86.8%, while Ctrl-24/GMO-24 (Fig. 7C), Ctrl-48/GMO-48 (Fig. 7D), Ctrl-24/GMO+IFD-24 (Fig. 7E), and Ctrl-48/GMO+IFD-48 (Fig. 7F) displayed explained variances greater than 90%. Also in this case, all the pairwise PCA scores plots highlighted a wider distribution of spectra from treated cell populations respect to control ones, particularly evident in the Ctrl-24/GMO+IFD-24 and Ctrl-48/GMO+IFD-48 comparisons. As regards PC1 loadings, a dominant contribution to the segregation of the groups was given by the lipid component of cells and nucleic acids (Fig. 8).

Figure 7

Figure 8

The height and, in some cases, the band height ratios, of specific peaks of interest were calculated from average Raman spectra and average ± SD Raman spectra of all experimental groups and statistically analysed. The Amide I band of proteins centred at 1652 cm^{-1} and the band centred at 1440 cm^{-1}, assigned to the CH$_2$ bending modes of lipid alkyl chains, were not taken into account, given the strong superimposition of the two main bands of glycerol monooleate molecule. Regarding lipids, the I$_{1740}$/I$_{1298}$ (representing lipid ester groups; Fig. 9A), displayed significantly higher values in GMO- and GMO+IFD-treated groups, both at 24 and 48 h; moreover, at 48 h, a significant increase respect to Ctrl was observed also in the IFD group; moreover, the I$_{1298}$ (representing lipid alkyl chains; Fig. 9B), and the I$_{1250}$/I$_{1298}$ (representing the degree of unsaturation of lipid alkyl chains; Fig. 9C) values showed a significant increase respect to Ctrl in all the experimental groups. As regards nucleic acids, the I$_{1578}$ (representing DNA adenines and guanines; Fig. 9D) value displayed a significant increase in IFD and GMO+IFD groups, both at 24 and 48 h, while no significant alteration was evidenced in

15

GMO-24 and GMO-48, suggesting that in the present experiment, this band is more appropriately assigned to furan ring vibrations; the I_{915}/I_{1084} (representing cellular RNA; Fig. 9E) showed a significant decrease respect to Ctrl groups in IFD and GMO-IFD, both at 24 and 48 h, while no significant decrease was detected in GMO groups; notably, in GMO+IFD-24 and GMO-IFD-48 the value of the ratio was close to zero; the I_{833}/I_{1084} (representing cellular B-DNA; Fig. 9F) value showed significantly lower values respect to Ctrl groups in IFD- and GMO-IFD-treated samples, both at 24 and 48 h, while no significant change was found in GMO groups.

Figure 9

4. Discussion

In a previous work, the potential tumor cell growth inhibitory effect of IFD, a natural furanosesquiterpene isolated from *S. olusatrum* [4], was tested on different human tumor cell lines [7]. The results showed an inhibitory activity on all tumor cell lines tested, with remarkable effects exerted on human colon carcinoma (HCT116), human breast adenocarcinoma (MDA-MB 231) and human glioblastoma multiforme (T98G) cell lines. Insights into the mechanisms of action of IFD on cancer cells showed that IFD inhibits breast cancer cell proliferation through apoptosis in a mitochondria-mediated pathway by regulating cyclin D1, CDK2, pRb, and Bcl-2 family proteins, as well as activating caspases and PARP [73]. IFD is also able to induce apoptosis in colon cancer cells in a time and concentration-dependent manner [6]. Against glioma cells, IFD exhibited anti-proliferative activity through inhibition of proliferation and induction of necrotic cell death. The mechanism of action of IFD on this cell line is not completely understood but the results suggest that IFD can cause ROS-dependent DNA damage [8]. Despite biological potential of IFD, the high lipophilicity along with a relatively low stability due to Cope rearrangement giving rise to a less active compound, make the perspective of its therapeutical use unlikely. Afterword, we exploited the possibility to encapsulate the lipophilic molecule IFD in liquid crystalline nanostructures (GMO) with the purpose of enhancing its stability and biological activity. *In vitro*, these nanoparticles were found

to better inhibit breast cancer MDA-MB 231 cells proliferation when compared to free IFD and this improvement could be due to the synergism between IFD and GMO hexosomes, likely because of differences in the internalization process [16,74].

In this study, human breast adenocarcinoma cell line, MDA-MB 231, treated with IFD alone and loaded into GMO nanoparticles, were analysed for the first time, by *in vitro* FTIRM and RMS, to widen the knowledge on the biochemical pathways activated by IFD and GMO+IFD. Relevant differences were highlighted in FTIRM and RMS spectral profiles of samples treated with IFD and GMO alone as well as with GMO+IFD. The group separation detected by PCA analysis of the FTIRM data shown in Figure 3 is clearly driven by the variations associated to the changes undergone by the stretching modes of alkyl groups, in the 3050-2800 cm^{-1} spectral region, as seen by the PC1 loading plots in Figure 4. Unfortunately, the presence of GMO inevitably affects the culture environment and also the biochemical composition of cells; hence, to avoid biases in the spectral analysis, the 3050-2800 cm^{-1} IR spectral range and the 1652 cm^{-1} and 1440 cm^{-1} Raman peaks, mostly influenced by the GMO presence, were not taken into account [75,76]. Nevertheless, it is noteworthy that the analysis of the Ctrl-24/IFD-24 and Ctrl-48/IFD-48 PCA comparisons showed a modification in the cellular lipid component attributable to IFD treatment, which is consistent with the onset of apoptosis induced by IFD and the subsequent accumulation of cytoplasmic lipid droplets [38,39,77,78].

To deeply investigate the response of cells to IFD and GMO+IFD and the onset of apoptotic processes, the analysis was focused in the 1350-900 cm^{-1} spectral region relative to cellular nucleic acids and carbohydrates. FTIRM and RMS highlighted for MDA-MB 231 cells treated with IFD a mechanism of apoptosis triggering, consistently with other studies [79,80]. DNA conformation showed to be affected by the IFD treatment, both alone and loaded into GMO nanoparticles, as suggested by the increase of the A-DNA form (IR A_{1240}/A_{1221} ratio) and the decrease of the B-DNA one (Raman I_{833}/I_{1084} ratio). Conversely, no cytotoxic activity involving DNA folding was detected after the treatment with GMO alone. It is known that changes in DNA conformation can be dependent on the hydration conditions [56], but, since cells were all maintained in the same hydration conditions,

it was possible to relate this transition from B- to A-form DNA to the drug treatment [58,81]. The IR A_{1087}/A_{TOT} and A_{967}/A_{TOT} ratios, respectively assigned to nucleic acids and DNA, revealed no change at 24 h, while a significant decrease was observed at 48 h both in IFD and GMO+IFD samples, respect to Ctrl ones: these results could suggest the onset of a mechanism of rearrangement and/or fragmentation of DNA, which may be related to the previously described misfolding of the DNA molecules [39,58,79]. This finding is also corroborated by the reduction of RNA amount detected in cells treated with IFD: both at 24 and 48 h, the IR A_{1120}/A_{TOT} and the Raman I_{915}/I_{1084} ratios displayed a significant decrease in IFD and GMO+IFD groups, with remarkably lower values in GMO+IFD-24 and GMO+IFD-48. This latter result seems to confirm the synergistic effect of the combination of IFD and GMO nanoparticles [16].

The decrease of carbohydrates and glycosylated compounds in IFD- and GMO+IFD-treated cells (IR A_{1054}/A_{TOT} ratio), at both 24 and 48 h, is consistent with the known mode of action of IFD, which targets cells not only through apoptosis triggering, and DNA fragmentation, but also lowering cell proliferation by inducing a cell cycle arrest in G2/M phase [79].

Finally, it was possible to include in the analysis the Raman bands centred at 1740, 1298 and 1250 cm^{-1}, assigned to lipids, since they were less influenced by GMO; hence the Raman I_{1740}/I_{1298}, I_{1298}, and I_{1250}/I_{1298} values related to lipids were considered. The increase of these ratios, especially at 48 h of treatment, also in IFD-24 and IFD-48 groups, suggests the onset of an apoptotic process and a condition of oxidative stress: the increase of the I_{1298} value may be indicative of the apoptosis-related accumulation of cytoplasmic lipid droplets, and the increase of the I_{1740}/I_{1298} and I_{1250}/I_{1298} values, respectively representing peroxidised lipids and unsaturated alkyl chains, suggests the activation of oxidative stress mechanisms [40,82], consistently with the known increase of ROS production induced by IFD [83].

5. Conclusions

In the present study, for the first time, an *in vitro* FTIRM and RMS combined approach was performed on MDA-MB 231 cells, treated with IFD, alone and loaded into GMO nanoparticles. The two vibrational techniques let evidence the anti-cancer effects of IFD, which was confirmed to rely on apoptosis triggering, ROS production, DNA fragmentation and cell cycle arrest in G2/M phase. Furthermore, the positive role of GMO nanoparticles as carrier of IFD was highlighted; in fact, the effects on cells treated with GMO+IFD, evidenced by infrared and Raman selected spectral features, appeared always more pronounced with respect to those observed with IFD alone.

In conclusion, this study confirms the positive effect of the encapsulation of IFD into GMO nanoparticles and the experimental approach used may pave the way to new investigations on different systems such as primary cancer cells and animal models on which these nanocarriers could be tested.

Credit author statement

Valentina Notarstefano: Investigation, Formal analysis, Writing – original draft; **Michel Pisani:** Conceptualization, Investigation, Writing – review and editing, Funding acquisition; **Massimo Bramucci:** Investigation, Resources, Writing – original draft; **Luana Quassinti:** Investigation, Resources; **Filippo Maggi:** Writing – original draft; **Lisa Vaccari:** Investigation, Writing – review and editing; **Marco Parlapiano:** Investigation; **Elisabetta Giorgini:** Conceptualization, Formal analysis, Writing – original draft, Writing - review and editing; **Paola Astolfi:** Conceptualization, Writing – original draft, Writing - review and editing

References

[1]   B. Armendáriz-Barragán, N. Zafar, W. Badri, S.A. Galindo-Rodríguez, D. Kabbaj, H. Fessi, A. Elaissari, Plant extracts: from encapsulation to application, Expert Opin. Drug Deliv. 13 (2016) 1165–1175. https://doi.org/10.1080/17425247.2016.1182487.

[2]   D.S. Fabricant, N.R. Farnsworth, The Value of Plants Used in Traditional Medicine for Drug Discovery, Environ. Health Perspect. 109 (2001) 69. https://doi.org/10.2307/3434847.

[3]   F. Maggi, L. Barboni, F. Papa, G. Caprioli, M. Ricciutelli, G. Sagratini, S. Vittori, A forgotten vegetable (Smyrnium olusatrum L., Apiaceae) as a rich source of isofuranodiene, Food Chem. 135 (2012) 2852–2862. https://doi.org/10.1016/j.foodchem.2012.07.027.

[4]   F. Maggi, F. Papa, C. Giuliani, L. Maleci Bini, A. Venditti, A. Bianco, M. Nicoletti, R. Iannarelli, G. Caprioli, G. Sagratini, M. Cortese, M. Ricciutelli, S. Vittori, Essential oil chemotypification and secretory structures of the neglected vegetable Smyrnium olusatrum L. (Apiaceae) growing in central Italy, Flavour Fragr. J. 30 (2015) 139–159. https://doi.org/10.1002/ffj.3221.

[5]   M. Buccioni, D. Dal Ben, C. Lambertucci, F. Maggi, F. Papa, A. Thomas, C. Santinelli, G. Marucci, Antiproliferative evaluation of isofuranodiene on breast and prostate cancer cell lines, Sci. World J. 2014 (2014). https://doi.org/10.1155/2014/264829.

[6]   L. Quassinti, F. Maggi, L. Barboni, M. Ricciutelli, M. Cortese, F. Papa, C. Garulli, C. Kalogris, S. Vittori, M. Bramucci, Wild celery (Smyrnium olusatrum L.) oil and isofuranodiene induce apoptosis in human colon carcinoma cells, Fitoterapia. 97 (2014) 133–141. https://doi.org/10.1016/j.fitote.2014.06.004.

[7]   L. Quassinti, M. Bramucci, G. Lupidi, L. Barboni, M. Ricciutelli, G. Sagratini, F. Papa, G. Caprioli, D. Petrelli, L.A. Vitali, S. Vittori, F. Maggi, In vitro biological activity of essential oils and isolated furanosesquiterpenes from the neglected vegetable Smyrnium olusatrum L. (Apiaceae), Food Chem. 138 (2013) 808–813. https://doi.org/10.1016/j.foodchem.2012.11.075.

[8]   A. Brunetti, O. Marinelli, M.B. Morelli, R. Iannarelli, C. Amantini, D. Russotti, G. Santoni,

F. Maggi, M. Nabissi, Isofuranodiene synergizes with temozolomide in inducing glioma cells death, Phytomedicine. 52 (2019) 51–59. https://doi.org/10.1016/j.phymed.2018.09.220.

[9]   Z. Zhong, W. Tan, X. Chen, Y. Wang, Furanodiene, a natural small molecule suppresses metastatic breast cancer cell migration and invasion in vitro, Eur. J. Pharmacol. 737 (2014) 1–10. https://doi.org/10.1016/j.ejphar.2014.04.043.

[10]   Z.-F.F. Zhong, W. Tan, K. Tian, H. Yu, W.-A.A. Qiang, Y.-T.T. Wang, Combined effects of furanodiene and doxorubicin on the migration and invasion of MDA-MB-231 breast cancer cells in vitro, Oncol. Rep. 37 (2017) 2016–2024. https://doi.org/10.3892/or.2017.5435.

[11]   J. Zhang, Y. He, J. Jiang, M. Li, C. Jin, L. Wang, D. Wang, In vitro and in vivo evaluation of folate-mediated PEGylated nanostructured lipid carriers for the efficient delivery of furanodiene, Drug Dev. Ind. Pharm. 43 (2017) 1610–1618. https://doi.org/10.1080/03639045.2017.1328429.

[12]   R. Pavela, L. Pavoni, G. Bonacucina, M. Cespi, N.G. Kavallieratos, L. Cappellacci, R. Petrelli, F. Maggi, G. Benelli, Rationale for developing novel mosquito larvicides based on isofuranodiene microemulsions, J. Pest Sci. (2004). 92 (2019) 909–921. https://doi.org/10.1007/s10340-018-01076-3.

[13]   F. Maggi, F. Papa, S. Pucciarelli, M. Bramucci, L. Quassinti, L. Barboni, D.D. Ben, A.T. Ramadori, C. Graiff, R. Galassi, Stabilization of the cyclodecadiene derivative isofuranodiene by silver (I) coordination. Mechanistic and biological aspects, Fitoterapia. 117 (2017) 52–60. https://doi.org/10.1016/j.fitote.2016.12.009.

[14]   Y. Zhao, C. Wang, A.H.L. Chow, K. Ren, T. Gong, Z. Zhang, Y. Zheng, Self-nanoemulsifying drug delivery system (SNEDDS) for oral delivery of Zedoary essential oil: Formulation and bioavailability studies, Int. J. Pharm. 383 (2010) 170–177. https://doi.org/10.1016/j.ijpharm.2009.08.035.

[15]   M. Cespi, L. Quassinti, D.R. Perinelli, M. Bramucci, R. Iannarelli, F. Papa, M. Ricciutelli, G. Bonacucina, G.F. Palmieri, F. Maggi, Microemulsions enhance the shelf-life and

processability of Smyrnium olusatrum L. essential oil, Flavour Fragr. J. 32 (2017) 159–164. https://doi.org/10.1002/ffj.3367.

[16]   M. Pisani, L. Quassinti, M. Bramucci, R. Galassi, F. Maggi, B. Rossi, A. Damin, P. Carloni, P. Astolfi, Nanostructured liquid crystalline particles as delivery vectors for isofuranodiene: Characterization and in-vitro anticancer activity, Colloids Surfaces B Biointerfaces. 192 (2020) 111050. https://doi.org/10.1016/j.colsurfb.2020.111050.

[17]   H. Qiu, M. Caffrey, The phase diagram of the monoolein/water system: Metastability and equilibrium aspects, Biomaterials. 21 (2000) 223–234. https://doi.org/10.1016/S0142-9612(99)00126-X.

[18]   Y. Da Dong, I. Larson, T. Hanley, B.J. Boyd, Bulk and dispersed aqueous phase behavior of phytantriol: Effect of vitamin E acetate and F127 polymer on liquid crystal nanostructure, Langmuir. 22 (2006) 9512–9518. https://doi.org/10.1021/la061706v.

[19]   N. Tran, X. Mulet, A.M. Hawley, C. Fong, J. Zhai, T.C. Le, J. Ratcliffe, C.J. Drummond, Manipulating the Ordered Nanostructure of Self-Assembled Monoolein and Phytantriol Nanoparticles with Unsaturated Fatty Acids, Langmuir. 34 (2018) 2764–2773. https://doi.org/10.1021/acs.langmuir.7b03541.

[20]   Y. Aota-Nakano, S.J. Li, M. Yamazaki, Effects of electrostatic interaction on the phase stability and structures of cubic phases of monoolein/oleic acid mixture membranes, Biochim. Biophys. Acta - Biomembr. 1461 (1999) 96–102. https://doi.org/10.1016/S0005-2736(99)00156-X.

[21]   T. Mishraki-Berkowitz, A. Aserin, N. Garti, Structural properties and release of insulin-loaded reverse hexagonal (HII) liquid crystalline mesophase, J. Colloid Interface Sci. 486 (2017) 184–193. https://doi.org/10.1016/j.jcis.2016.09.074.

[22]   M. Fornasier, R. Pireddu, A. Del Giudice, C. Sinico, T. Nylander, K. Schillén, L. Galantini, S. Murgia, Tuning lipid structure by bile salts: Hexosomes for topical administration of catechin, Colloids Surfaces B Biointerfaces. 199 (2021) 111564.

https://doi.org/10.1016/j.colsurfb.2021.111564.

[23] P. Astolfi, M. Pisani, E. Giorgini, B. Rossi, A. Damin, F. Vita, O. Francescangeli, L. Luciani, R. Galassi, Synchrotron Characterization of Hexagonal and Cubic Lipidic Phases Loaded with Azolate/Phosphane Gold(I) Compounds: A New Approach to the Uploading of Gold(I)-Based Drugs, Nanomaterials. 10 (2020) 1851. https://doi.org/10.3390/nano10091851.

[24] J. Zhai, C. Fong, N. Tran, C.J. Drummond, Non-Lamellar Lyotropic Liquid Crystalline Lipid Nanoparticles for the Next Generation of Nanomedicine, ACS Nano. 13 (2019) 6178–6206. https://doi.org/10.1021/acsnano.8b07961.

[25] H.M.G. Barriga, M.N. Holme, M.M. Stevens, Cubosomes: The Next Generation of Smart Lipid Nanoparticles?, Angew. Chemie - Int. Ed. 58 (2019) 2958–2978. https://doi.org/10.1002/anie.201804067.

[26] A. Angelova, V.M. Garamus, B. Angelov, Z. Tian, Y. Li, A. Zou, Advances in structural design of lipid-based nanoparticle carriers for delivery of macromolecular drugs, phytochemicals and anti-tumor agents, Adv. Colloid Interface Sci. 249 (2017) 331–345. https://doi.org/10.1016/j.cis.2017.04.006.

[27] A. Angelova, B. Angelov, R. Mutafchieva, S. Lesieur, P. Couvreur, Self-Assembled multicompartment liquid crystalline lipid carriers for protein, peptide, and nucleic acid drug delivery, Acc. Chem. Res. 44 (2011) 147–156. https://doi.org/10.1021/ar100120v.

[28] G. Zhen, T.M. Hinton, B.W. Muir, S. Shi, M. Tizard, K.M. McLean, P.G. Hartley, P. Gunatillake, Glycerol monooleate-based nanocarriers for siRNA delivery in vitro, Mol. Pharm. 9 (2012) 2450–2457. https://doi.org/10.1021/mp200662f.

[29] H. Kim, C. Leal, Cuboplexes: Topologically Active siRNA Delivery, ACS Nano. 9 (2015) 10214–10226. https://doi.org/10.1021/acsnano.5b03902.

[30] J. Zhai, R.B. Luwor, N. Ahmed, R. Escalona, F.H. Tan, C. Fong, J. Ratcliffe, J.A. Scoble, C.J. Drummond, N. Tran, Paclitaxel-Loaded Self-Assembled Lipid Nanoparticles as Targeted Drug Delivery Systems for the Treatment of Aggressive Ovarian Cancer, ACS

Appl. Mater. Interfaces. 10 (2018) 25174–25185. https://doi.org/10.1021/acsami.8b08125.

[31]   N.R. Rarokar, P.B. Khedekar, A.P. Bharne, M.J. Umekar, Development of self-assembled

nanocarriers to enhance antitumor efficacy of docetaxel trihydrate in MDA-MB-231 cell line,

Int. J. Biol. Macromol. 125 (2019) 1056–1068.

https://doi.org/10.1016/j.ijbiomac.2018.12.130.

[32]   C. Caltagirone, M. Arca, A.M. Falchi, V. Lippolis, V. Meli, M. Monduzzi, T. Nylander, A.

Rosa, J. Schmidt, Y. Talmon, S. Murgia, Solvatochromic fluorescent BODIPY derivative as

imaging agent in camptothecin loaded hexosomes for possible theranostic applications, RSC

Adv. 5 (2015) 23443–23449. https://doi.org/10.1039/c5ra01025j.

[33]   E. Nazaruk, A. Majkowska-Pilip, R. Bilewicz, Lipidic Cubic-Phase Nanoparticles—

Cubosomes for Efficient Drug Delivery to Cancer Cells, Chempluschem. 82 (2017) 570–575.

https://doi.org/10.1002/cplu.201600534.

[34]   P. Astolfi, E. Giorgini, V. Gambini, B. Rossi, L. Vaccari, F. Vita, O. Francescangeli, C.

Marchini, M. Pisani, Lyotropic Liquid-Crystalline Nanosystems as Drug Delivery Agents for

5-Fluorouracil: Structure and Cytotoxicity, Langmuir. 33 (2017).

https://doi.org/10.1021/acs.langmuir.7b03173.

[35]   P. Astolfi, E. Giorgini, F.C. Adamo, F. Vita, S. Logrippo, O. Francescangeli, M. Pisani,

Effects of a cationic surfactant incorporation in phytantriol bulk cubic phases and dispersions

loaded with the anticancer drug 5-fluorouracil, J. Mol. Liq. 286 (2019).

https://doi.org/10.1016/j.molliq.2019.110954.

[36]   J. Van Meerloo, G.J.L. Kaspers, J. Cloos, Cell sensitivity assays: The MTT assay, Methods

Mol. Biol. 731 (2011) 237–245. https://doi.org/10.1007/978-1-61779-80-5_20.

[37]   W. Strober, Trypan blue exclusion test of cell viability., Curr. Protoc. Immunol. Appendix 3

(2001). https://doi.org/10.1002/0471142735.ima03bs21.

[38]   E. Giorgini, S. Sabbatini, R. Rocchetti, V. Notarstefano, C. Rubini, C. Conti, G. Orilisi, E.

Mitri, D.E. Bedolla, L. Vaccari, In vitro FTIR microspectroscopy analysis of primary oral

squamous carcinoma cells treated with cisplatin and 5-fluorouracil: a new spectroscopic approach for studying the drug–cell interaction, Analyst. 143 (2018) 3317–3326. https://doi.org/10.1039/C8AN00602D.

[39]   V. Notarstefano, S. Sabbatini, C. Pro, A. Belloni, G. Orilisi, C. Rubini, H.J. Byrne, L. Vaccari, E. Giorgini, Exploiting fourier transform infrared and Raman microspectroscopies on cancer stem cells from oral squamous cells carcinoma: new evidence of acquired cisplatin chemoresistance, Analyst. 145 (2020) 8038–8049. https://doi.org/10.1039/D0AN01623C.

[40]   V. Notarstefano, G. Gioacchini, H.J.H.J. Byrne, C. Zacà, E. Sereni, L. Vaccari, A. Borini, O. Carnevali, E. Giorgini, Vibrational characterization of granulosa cells from patients affected by unilateral ovarian endometriosis: New insights from infrared and Raman microspectroscopy, Spectrochim. Acta Part A Mol. Biomol. Spectrosc. 212 (2019) 206–214. https://doi.org/10.1016/j.saa.2018.12.054.

[41]   G. Benelli, R. Pavela, A. Canale, M. Nicoletti, R. Petrelli, L. Cappellacci, R. Galassi, F. Maggi, Isofuranodiene and germacrone from Smyrnium olusatrum essential oil as acaricides and oviposition inhibitors against Tetranychus urticae: impact of chemical stabilization of isofuranodiene by interaction with silver triflate, J. Pest Sci. (2004). 90 (2017) 693–699. https://doi.org/10.1007/s10340-016-0829-5.

[42]   A.D. Meade, C. Clarke, F. Draux, G.D. Sockalingum, M. Manfait, F.M. Lyng, H.J. Byrne, Studies of chemical fixation effects in human cell lines using Raman microspectroscopy, Anal. Bioanal. Chem. 396 (2010) 1781–1791. https://doi.org/10.1007/s00216-009-3411-7.

[43]   M.J. Baker, J. Trevisan, P. Bassan, R. Bhargava, H.J. Butler, K.M. Dorling, P.R. Fielden, S.W. Fogarty, N.J. Fullwood, K.A. Heys, C. Hughes, P. Lasch, P.L. Martin-Hirsch, B. Obinaju, G.D. Sockalingum, J. Sulé-Suso, R.J. Strong, M.J. Walsh, B.R. Wood, P. Gardner, F.L. Martin, Using Fourier transform IR spectroscopy to analyze biological materials, Nat. Protoc. 9 (2014) 1771–1791. https://doi.org/10.1038/nprot.2014.110.

[44]   L. Vaccari, G. Birarda, L. Businaro, S. Pacor, G. Grenci, Infrared Microspectroscopy of Live

Cells in Microfluidic Devices (MD-IRMS): Toward a Powerful Label-Free Cell-Based

Assay, Anal. Chem. 84 (2012) 4768–4775. https://doi.org/10.1021/ac300313x.

[45] V. Notarstefano, S. Sabbatini, C. Conti, M. Pisani, P. Astolfi, C. Pro, C. Rubini, L. Vaccari, E. Giorgini, Investigation of human pancreatic cancer tissues by Fourier Transform Infrared Hyperspectral Imaging, J. Biophotonics. 13 (2020) 1–10. https://doi.org/10.1002/jbio.201960071.

[46] J. Gustafsson, H. Ljusberg-Wahren, M. Almgren, K. Larsson, Submicron particles of reversed lipid phases in water stabilized by a nonionic amphiphilic polymer, Langmuir. 13 (1997) 6964–6971. https://doi.org/10.1021/la970566+.

[47] C. V. Kulkarni, W. Wachter, G. Iglesias-Salto, S. Engelskirchen, S. Ahualli, Monoolein: A magic lipid?, Phys. Chem. Chem. Phys. 13 (2011) 3004–3021. https://doi.org/10.1039/c0cp01539c.

[48] T. Kaasgaard, C.J. Drummond, Ordered 2-D and 3-D nanostructured amphiphile self-assembly materials stable in excess solvent, Phys. Chem. Chem. Phys. 8 (2006) 4957–4975. https://doi.org/10.1039/b609510k.

[49] E. Giorgini, S. Sabbatini, C. Conti, C. Rubini, R. Rocchetti, M. Re, L. Vaccari, E. Mitri, V. Librando, Vibrational mapping of sinonasal lesions by Fourier transform infrared imaging spectroscopy, J. Biomed. Opt. 20 (2015) 125003. https://doi.org/10.1117/1.JBO.20.12.125003.

[50] V. Notarstefano, G. Gioacchini, E. Giorgini, N. Montik, A. Ciavattini, A.R. Polidori, F.A. Candela, L. Vaccari, M. Cignitti, O. Carnevali, The Impact of Controlled Ovarian Stimulation Hormones on the Metabolic State and Endocannabinoid System of Human Cumulus Cells, Int. J. Mol. Sci. 21 (2020) 7124. https://doi.org/10.3390/ijms21197124.

[51] G. Gioacchini, V. Notarstefano, E. Sereni, C. Zacà, G. Coticchio, E. Giorgini, L. Vaccari, O. Carnevali, A. Borini, Does the molecular and metabolic profile of human granulosa cells correlate with oocyte fate? New insights by Fourier transform infrared microspectroscopy

analysis, MHR Basic Sci. Reprod. Med. 24 (2018) 521–532.

https://doi.org/10.1093/molehr/gay035.

[52] A.C.S. Talari, M.A.G. Martinez, Z. Movasaghi, S. Rehman, I.U. Rehman, Advances in

Fourier transform infrared (FTIR) spectroscopy of biological tissues, Appl. Spectrosc. Rev.

52 (2017) 456–506. https://doi.org/10.1080/05704928.2016.1230863.

[53] P. Zucchiatti, E. Mitri, S. Kenig, F. Billè, G. Kourousias, D.E. Bedolla, L. Vaccari,

Contribution of Ribonucleic Acid (RNA) to the Fourier Transform Infrared (FTIR) Spectrum

of Eukaryotic Cells, Anal. Chem. 88 (2016) 12090–12098.

https://doi.org/10.1021/acs.analchem.6b02744.

[54] M. Weniger, K.C. Honselmann, A.S. Liss, The Extracellular Matrix and Pancreatic Cancer:

A Complex Relationship., Cancers (Basel). 10 (2018) 316.

https://doi.org/10.3390/cancers10090316.

[55] D. Ghosh, S.K. Dey, C. Saha, Mutation Induced Conformational Changes in Genomic DNA

from Cancerous K562 Cells Influence Drug-DNA Binding Modes, PLoS One. 9 (2014)

e84880. https://doi.org/10.1371/journal.pone.0084880.

[56] D.R. Whelan, K.R. Bambery, P. Heraud, M.J. Tobin, M. Diem, D. McNaughton, B.R. Wood,

Monitoring the reversible B to A-like transition of DNA in eukaryotic cells using Fourier

transform infrared spectroscopy, Nucleic Acids Res. 39 (2011) 5439–5448.

https://doi.org/10.1093/nar/gkr175.

[57] V. Notarstefano, S. Sabbatini, M. Sabbatini, A. Arrais, A. Belloni, C. Pro, L. Vaccari, D.

Osella, E. Giorgini, Hyperspectral characterization of the MSTO-211H cell spheroid model :

A FPA – FTIR imaging approach, Clin. Spectrosc. 3 (2021) 100011.

https://doi.org/10.1016/j.clispe.2021.100011.

[58] A. Mignolet, A. Derenne, M. Smolina, B.R. Wood, E. Goormaghtigh, FTIR spectral

signature of anticancer drugs. Can drug mode of action be identified?, Biochim. Biophys.

Acta - Proteins Proteomics. 1864 (2016) 85–101.

https://doi.org/10.1016/j.bbapap.2015.08.010.

[59] B. Kann, H.L. Offerhaus, M. Windbergs, C. Otto, Raman microscopy for cellular investigations — From single cell imaging to drug carrier uptake visualization, Adv. Drug Deliv. Rev. 89 (2015) 71–90. https://doi.org/10.1016/j.addr.2015.02.006.

[60] A.C.S. Talari, Z. Movasaghi, S. Rehman, I.U. Rehman, Raman spectroscopy of biological tissues, Appl. Spectrosc. Rev. 50 (2015) 46–111. https://doi.org/10.1080/05704928.2014.923902.

[61] E. Efeoglu, M.A. Maher, A. Casey, H.J. Byrne, Toxicological assessment of nanomaterials: the role of in vitro Raman microspectroscopic analysis, Anal. Bioanal. Chem. 410 (2018) 1631–1646. https://doi.org/10.1007/s00216-017-0812-x.

[62] R. Geitner, J. Kötteritzsch, M. Siegmann, T.W. Bocklitz, M.D. Hager, U.S. Schubert, S. Gräfe, B. Dietzek, M. Schmitt, J. Popp, Two-dimensional Raman correlation spectroscopy reveals molecular structural changes during temperature-induced self-healing in polymers based on the Diels–Alder reaction, Phys. Chem. Chem. Phys. 17 (2015) 22587–22595. https://doi.org/10.1039/C5CP02151K.

[63] A. Reyer, G. Tondi, R.J.F. Berger, A. Petutschnigg, M. Musso, Raman spectroscopic investigation of tannin-furanic rigid foams, Vib. Spectrosc. 84 (2016) 58–66. https://doi.org/10.1016/j.vibspec.2016.03.005.

[64] Z. Farhane, F. Bonnier, H.J. Byrne, Monitoring doxorubicin cellular uptake and trafficking using in vitro Raman microspectroscopy: short and long time exposure effects on lung cancer cell lines, Anal. Bioanal. Chem. 409 (2017) 1333–1346. https://doi.org/10.1007/s00216-016-0065-0.

[65] H.K. Yosef, T. Frick, M.K. Hammoud, A. Maghnouj, S. Hahn, K. Gerwert, S.F. El-Mashtoly, Exploring the efficacy and cellular uptake of sorafenib in colon cancer cells by Raman micro-spectroscopy, Analyst. 143 (2018) 6069–6078. https://doi.org/10.1039/C8AN02029A.

[66] S. Managò, G. Zito, A.C. De Luca, Raman microscopy based sensing of leukemia cells: A review, Opt. Laser Technol. 108 (2018) 7–16. https://doi.org/10.1016/j.optlastec.2018.06.034.

[67] Z. Farhane, F. Bonnier, A. Casey, A. Maguire, L. O'Neill, H.J. Byrne, Cellular discrimination using in vitro Raman micro spectroscopy: the role of the nucleolus, Analyst. 140 (2015) 5908–5919. https://doi.org/10.1039/C5AN01157D.

[68] Z. Farhane, H. Nawaz, F. Bonnier, H.J. Byrne, In vitro label-free screening of chemotherapeutic drugs using Raman microspectroscopy: Towards a new paradigm of spectralomics, J. Biophotonics. 11 (2018) e201700258. https://doi.org/10.1002/jbio.201700258.

[69] J.W. Chan, D.S. Taylor, T. Zwerdling, S.M. Lane, K. Ihara, T. Huser, Micro-Raman Spectroscopy Detects Individual Neoplastic and Normal Hematopoietic Cells, Biophys. J. 90 (2006) 648–656. https://doi.org/10.1529/biophysj.105.066761.

[70] L. Teng, X. Wang, X. Wang, H. Gou, L. Ren, T. Wang, Y. Wang, Y. Ji, W.E. Huang, J. Xu, Label-free, rapid and quantitative phenotyping of stress response in E. coli via ramanome, Sci. Rep. 6 (2016). https://doi.org/10.1038/srep34359.

[71] I.R. Ramos, A.D. Meade, O. Ibrahim, H.J. Byrne, M. McMenamin, M. McKenna, A. Malkin, F.M. Lyng, Raman spectroscopy for cytopathology of exfoliated cervical cells, Faraday Discuss. 187 (2016) 187–198. https://doi.org/10.1039/C5FD00197H.

[72] N. Li, D. Chen, Y. Xu, S. Liu, H. Zhang, Confocal Raman micro-spectroscopy for rapid and label-free detection of maleic acid-induced variations in human sperm, Biomed. Opt. Express. 5 (2014) 1690. https://doi.org/10.1364/BOE.5.001690.

[73] Z. Zhong, Y. Dang, X. Yuan, W. Guo, Y. Li, W. Tan, J. Cui, J. Lu, Q. Zhang, X. Chen, Y. Wang, Furanodiene, a Natural Product, Inhibits Breast Cancer Growth Both in vitro and in vivo, Cell. Physiol. Biochem. 30 (2012) 778–790. https://doi.org/10.1159/000341457.

[74] N. Tran, X. Mulet, A.M. Hawley, T.M. Hinton, S.T. Mudie, B.W. Muir, E.C. Giakoumatos,

L.J. Waddington, N.M. Kirby, C.J. Drummond, Nanostructure and cytotoxicity of self-assembled monoolein-capric acid lyotropic liquid crystalline nanoparticles, RSC Adv. 5 (2015) 26785–26795. https://doi.org/10.1039/c5ra02604k.

[75] A. Rosa, S. Murgia, D. Putzu, V. Meli, A.M. Falchi, Monoolein-based cubosomes affect lipid profile in HeLa cells, Chem. Phys. Lipids. 191 (2015) 96–105. https://doi.org/10.1016/j.chemphyslip.2015.08.017.

[76] A.M. Falchi, A. Rosa, A. Atzeri, A. Incani, S. Lampis, V. Meli, C. Caltagirone, S. Murgia, Effects of monoolein-based cubosome formulations on lipid droplets and mitochondria of HeLa cells, Toxicol. Res. (Camb). 4 (2015) 1025–1036. https://doi.org/10.1039/c5tx00078e.

[77] Q. Kong, Y. Ma, J. Yu, X. Chen, Predicted molecular targets and pathways for germacrone, curdione, and furanodiene in the treatment of breast cancer using a bioinformatics approach, Sci. Rep. 7 (2017) 15543. https://doi.org/10.1038/s41598-017-15812-9.

[78] U. Zelig, J. Kapelushnik, R. Moreh, S. Mordechai, I. Nathan, Diagnosis of cell death by means of infrared spectroscopy, Biophys. J. 97 (2009) 2107–2114. https://doi.org/10.1016/j.bpj.2009.07.026.

[79] Y. Xiao, Y. Feng-Qing, L. Shao-Ping, G. Jian-Li, H. Guang, L. Sin-Cheng, C.L. Emilia, F. Kwok-Pui, W. Yi-Tao, L.M.-Y. Simon, Furanodiene induces G2/M cell cycle arrest and apoptosis through MAPK signaling and mitochondria-caspase pathway in human hepatocellular carcinoma cells, Cancer Biol. Ther. 6 (2007) 1044–1050. https://doi.org/10.4161/cbt.6.7.4317.

[80] Z.-F. Zhong, H.-B. Yu, C.-M. Wang, W.-A. Qiang, S.-P. Wang, J.-M. Zhang, H. Yu, L. Cui, T. Wu, D.-Q. Li, Y.-T. Wang, Furanodiene Induces Extrinsic and Intrinsic Apoptosis in Doxorubicin-Resistant MCF-7 Breast Cancer Cells via NF-κB-Independent Mechanism, Front. Pharmacol. 8 (2017) 1–12. https://doi.org/10.3389/fphar.2017.00648.

[81] V. Notarstefano, A. Belloni, S. Sabbatini, C. Pro, G. Orilisi, R. Monterubbianesi, V. Tosco, H.J. Byrne, L. Vaccari, E. Giorgini, Cytotoxic Effects of 5-Azacytidine on Primary Tumour

Cells and Cancer Stem Cells from Oral Squamous Cell Carcinoma: An In Vitro FTIRM Analysis, Cells. 10 (2021) 2127. https://doi.org/10.3390/cells10082127.

[82]   B. Vileno, S. Jeney, A. Sienkiewicz, P.R. Marcoux, L.M. Miller, L. Forró, Evidence of lipid peroxidation and protein phosphorylation in cells upon oxidative stress photo-generated by fullerols, Biophys. Chem. 152 (2010) 164–169. https://doi.org/10.1016/j.bpc.2010.09.004.

[83]   X.-Y. Zhu, D.-W. Guo, Q.-C. Lao, Y.-Q. Xu, Z.-K. Meng, B. Xia, H. Yang, C.-Q. Li, P. Li, Sensitization and synergistic anti-cancer effects of Furanodiene identified in zebrafish models, Sci. Rep. 9 (2019) 4541. https://doi.org/10.1038/s41598-019-40866-2.
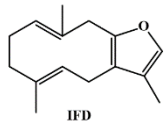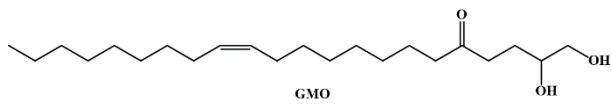
Chart. Chemical structure of monoolein (GMO) and isofuranodiene (IFD)
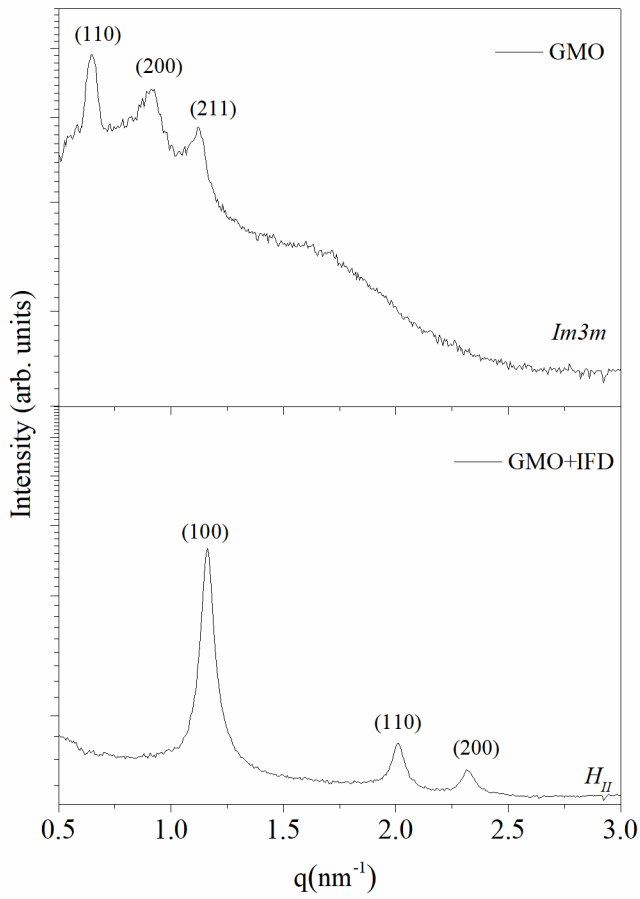
Figure 1. Synchrotron x-rays diffraction patterns of empty and IFD loaded GMO nanoparticles
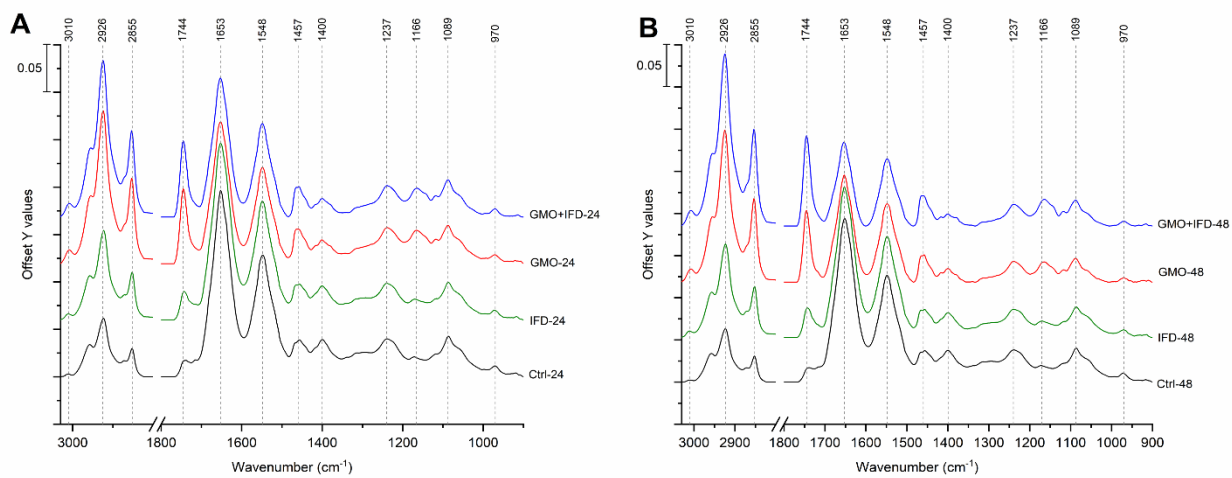
Figure 2. Average IR spectra in the 3050-2800 cm^{-1} and 1800-900 cm^{-1} spectral ranges of: (A) Ctrl-24 (black), IFD-24 (green), GMO-24 (red), and GMO+IFD-24 (blue); (B) Ctrl-48 (black), IFD-48 (green), GMO-48 (red), and GMO+IFD-48 (blue). For a better viewing, spectra are off set along y-axis. Dotted vertical lines indicate meaningful bands.
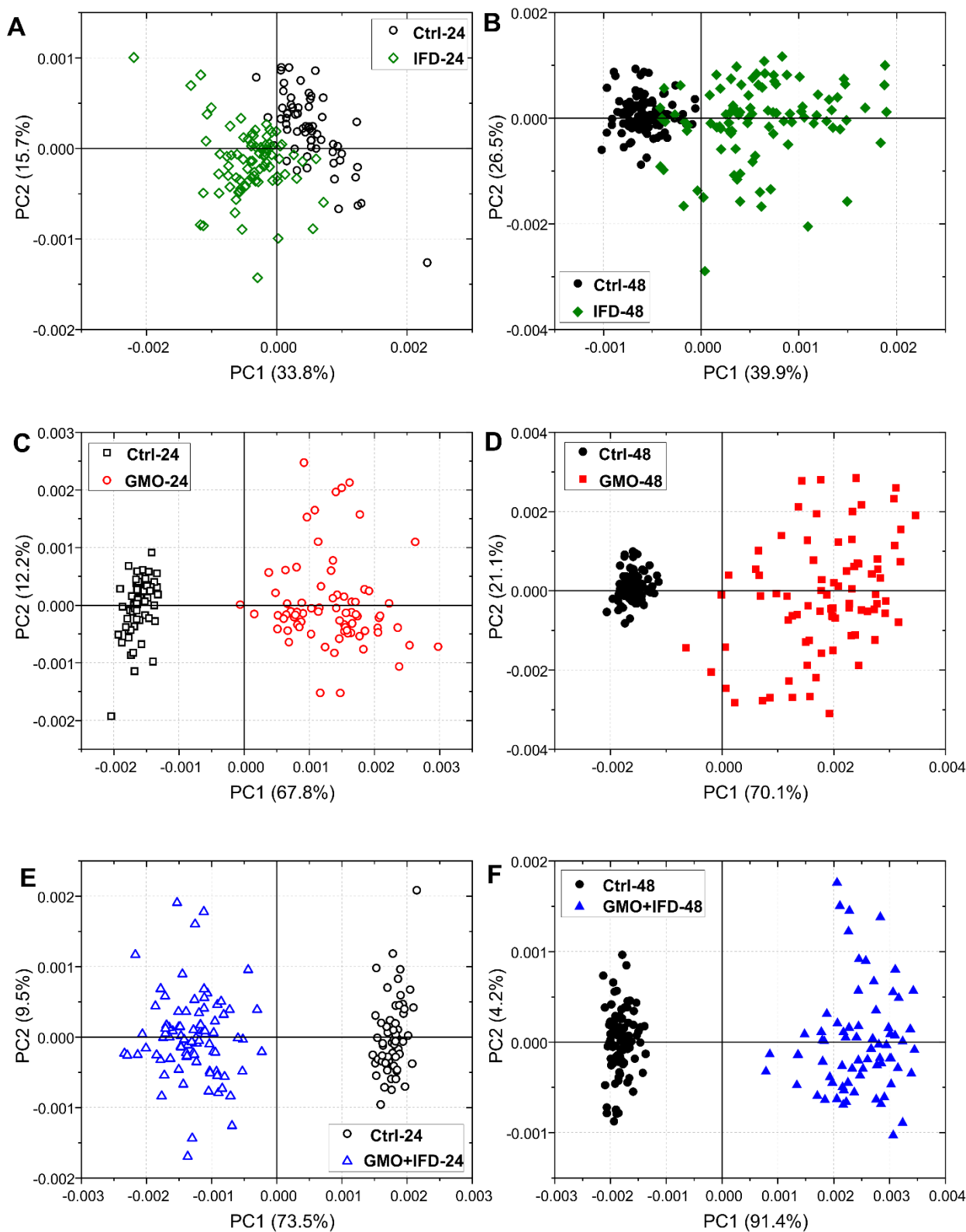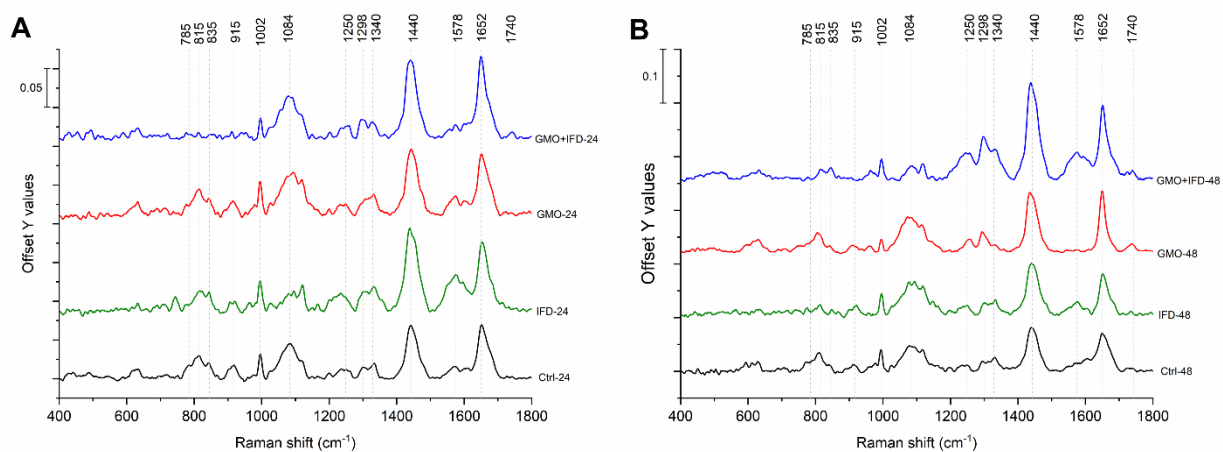
Figure 3. Pairwise PCA scores plots of the following IR populations: A) Ctrl-24/IFD-24; B) Ctrl-48/IFD-48; C) Ctrl-24/GMO-24; D) Ctrl-48/GMO-48; E) Ctrl-24/GMO+IFD-24, and F) Ctrl-48/GMO+IFD-48.
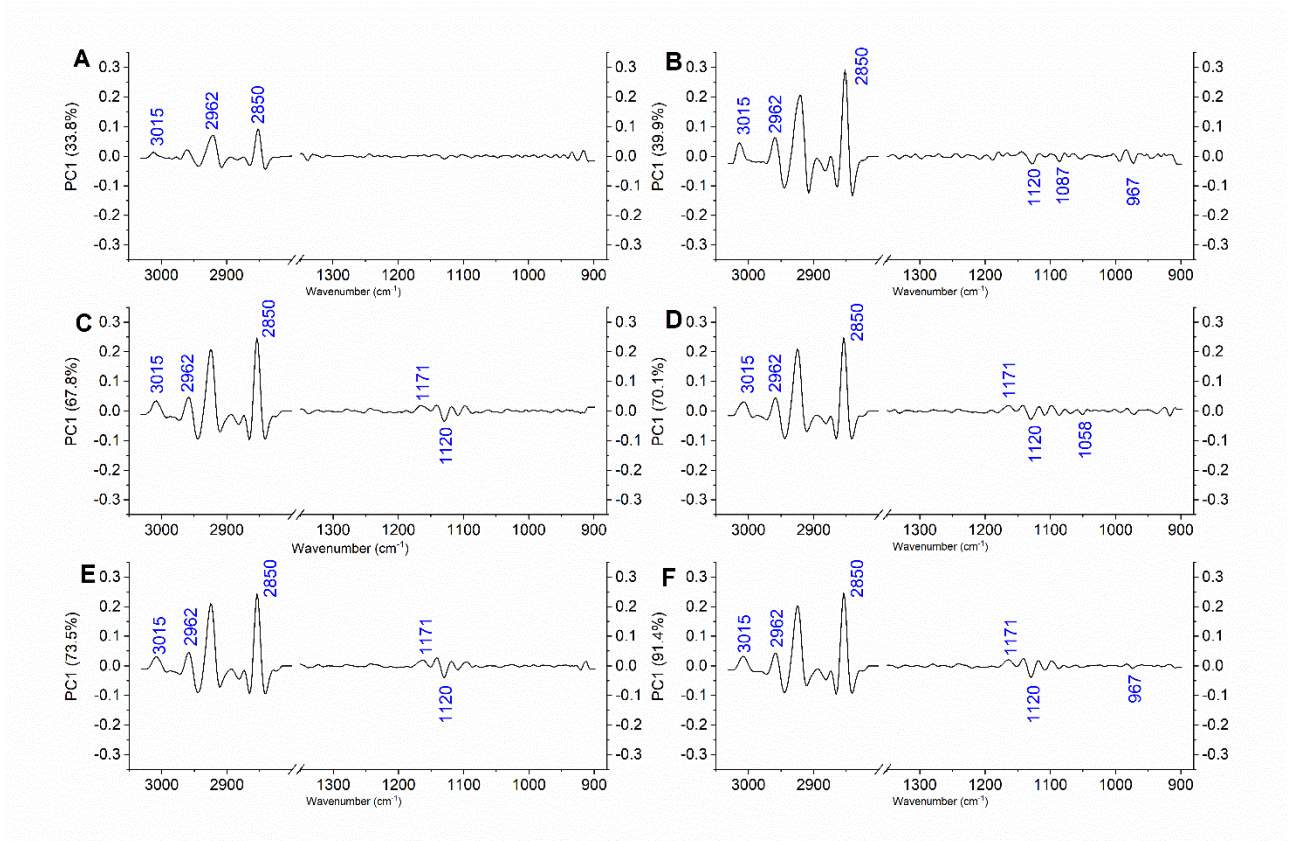
Figure 4. PC1 loading spectra of the following comparisons: A) Ctrl-24/IFD-24; B) Ctrl-48/IFD-48; C) Ctrl-24/GMO-24; D) Ctrl-48/GMO-48; E) Ctrl-24/GMO+IFD-24, and F) Ctrl-48/GMO+IFD-48. Blue labels indicate the most relevant IR discriminant features.
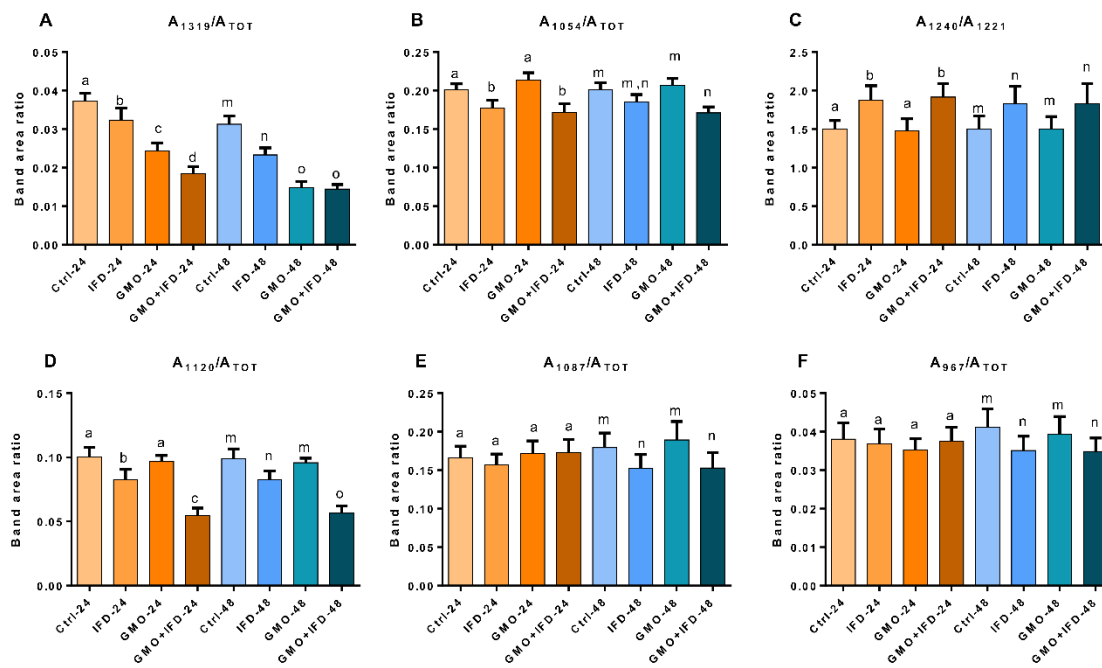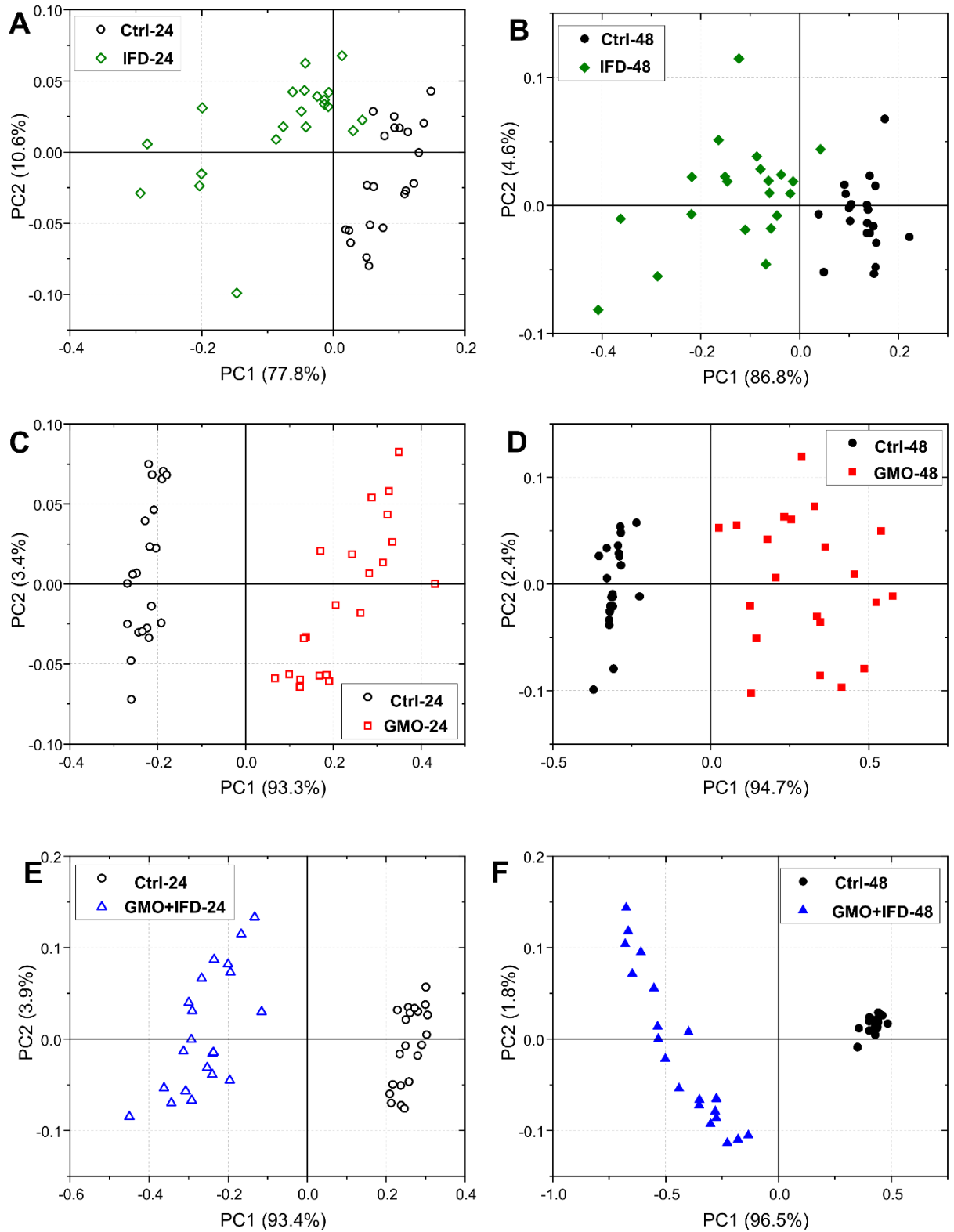
Figure 5. Univariate statistical analysis of the following band area ratios calculated for Ctrl-24, IFD-24, GMO-24, GMO+IFD-24, Ctrl-48, IFD-48, GMO-48, and GMO+IFD-48 groups: (A) A_{1319}/A_{TOT}, (B) A_{1054}/A_{TOT}, (C) A_{1240}/A_{1221}, (D) A_{1120}/A_{TOT}, (E) A_{1087}/A_{TOT}, and (F) A_{967}/A_{TOT}. Band area ratios are reported as mean±S.D. One-way ANOVA, followed by Tukey's multiple comparisons test, was performed to evaluate statistically significant differences among the experimental groups. Different letters above histograms indicate statistically significant differences among groups ($p<0.05$).

Figure 6. Average Raman spectra in the 400-1800 cm^{-1} spectral range of: (A) Ctrl-24 (black), IFD-24 (green), GMO-24 (red), and GMO+IFD-24 (blue); (B) Ctrl-48 (black), IFD-48 (green), GMO-48 (red), and GMO+IFD-48 (blue). For a better viewing, spectra are off set along y-axis.

Figure 7. Pairwise PCA scores plots of the following Raman populations: A) Ctrl-24/IFD-24; B) Ctrl-48/IFD-48; C) Ctrl-24/GMO-24; D) Ctrl-48/GMO-48; E) Ctrl-24/GMO+IFD-24, and F) Ctrl-48/GMO+IFD-48.
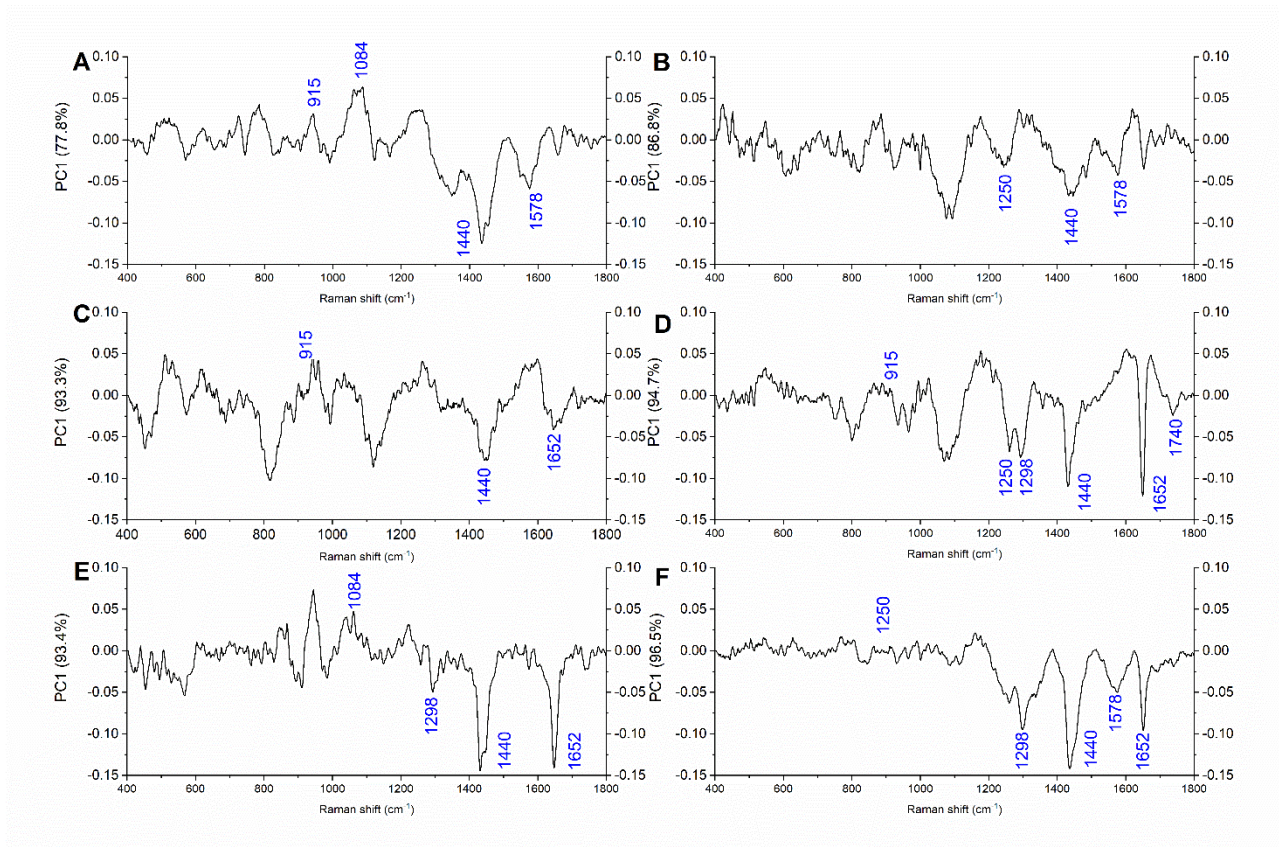
Figure 8. PC1 loading spectra of the following comparisons: A) Ctrl-24/IFD-24; B) Ctrl-48/IFD-48; C) Ctrl-24/GMO-24; D) Ctrl-48/GMO-48; E) Ctrl-24/GMO+IFD-24, and F) Ctrl-48/GMO+IFD-48. Blue labels indicate the most relevant Raman discriminant features.
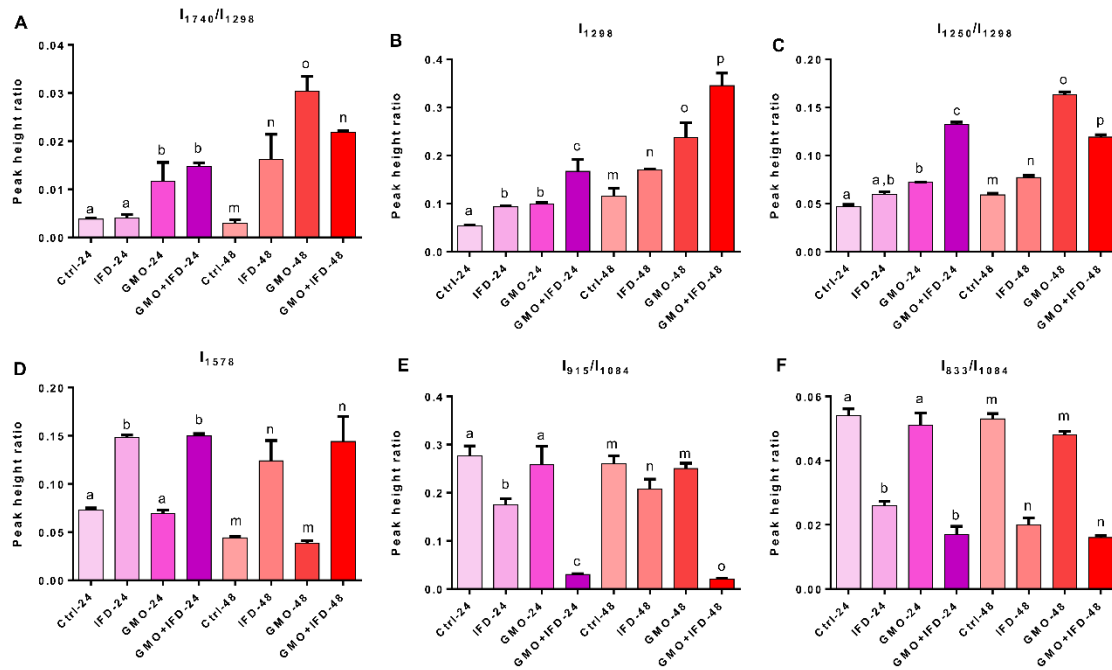
Figure 9. Univariate statistical analysis of the following peak height values and ratios calculated for Ctrl-24, IFD-24, GMO-24, GMO+IFD-24, Ctrl-48, IFD-48, GMO-48, and GMO+IFD-48 groups: (A) I_{1740}/I_{1298}, (B) I_{1298}, (C) I_{1250}/I_{1298}, (D) I_{1578}, (E) I_{915}/I_{1084}, and (F) I_{833}/I_{1084}. Values are reported as mean±S.D. One-way ANOVA, followed by Tukey's multiple comparisons test, was performed to evaluate statistically significant differences among the experimental groups. Different letters above histograms indicate statistically significant differences among groups ($p<0.05$).